




Evaluation of Electrochemical and Antimicrobial Efficacy of Green Synthesized Silver Functionalized Reduced Graphene Oxide Nanocomposites

Arpana Parihar¹ · Nishant Kumar Choudhary² · Palak Sharma² · Raju Khan^{1,3}  · Ayush Gupta⁴

Received: 19 January 2024 / Accepted: 3 April 2024

© The Author(s), under exclusive licence to Springer Science+Business Media, LLC, part of Springer Nature 2024

Abstract

The emergence of antibiotic-resistant strains and delayed results of established diagnostic techniques at the point of care is a substantial barrier to effective antibiotic management of infection. Due to the delays in sample collection, bacterial culture, processing, and antibiotic susceptibility testing, antibiotics have been used indiscriminately, facilitating the growth of infections resistant to certain antibiotics. The advent of nanotechnology at the interface of material chemistry has facilitated us with the tools to synthesize novel anti-microbial agents. Herein, we report the biogenesis of silver and its graphene oxide nanocomposite and the evaluation of their electrochemical and antibacterial properties. The reduced graphene oxide silver nanomaterial was successfully synthesized using the *Lactobacillus* biomass in an environmentally friendly, simple, and scalable manner, acting as a reducing and nanocomposite stabilizing agent. The nanocomposites were characterized using TEM, EDX, XRD, UV–Vis, Raman, FT-IR, and FESEM which efficaciously confirm the synthesis of the nanocomposites. The synthesized material was further characterized by CV, DPV, and EIS-based electrochemical techniques which suggest their feasible electrochemical properties. The antimicrobial susceptibility assay showed that Ag-rGO nanocomposite possesses excellent antimicrobial activity as compared to AgNPs. The green synthesis reported in this work led to the production of water-dispersible, cost-effective, high-purity reduced graphene oxide silver nanocomposites having good electrochemical and antimicrobial properties.

✉ Raju Khan
khan.raju@gmail.com

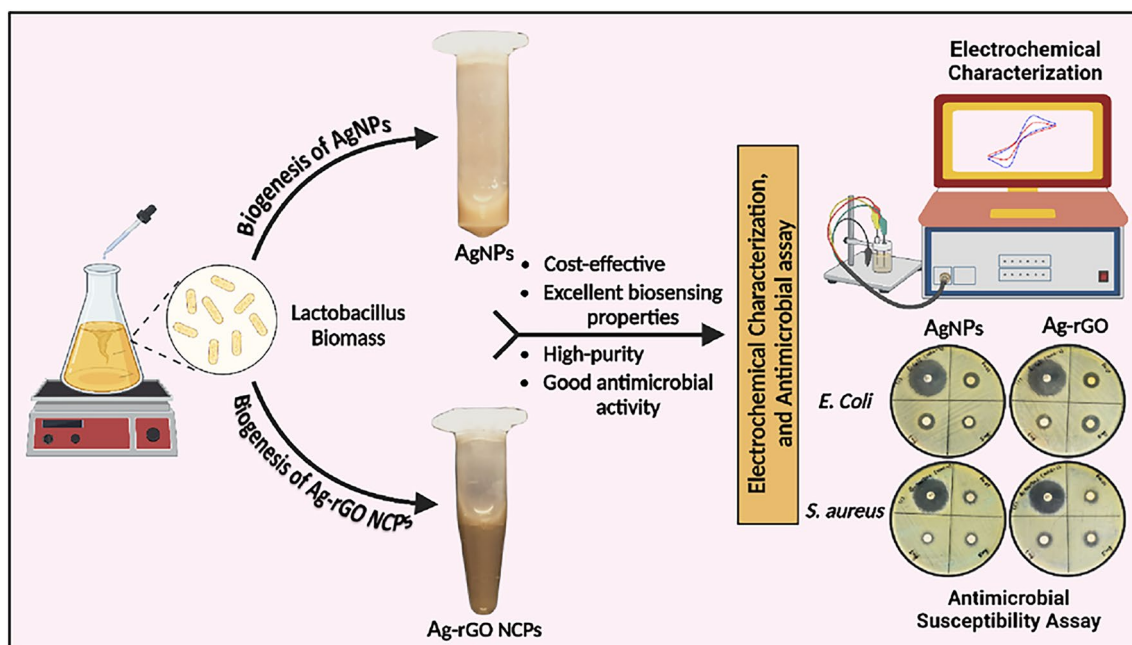
¹ CSIR-Advanced Materials and Processes Research Institute (AMPRI), Hoshangabad Road, Bhopal, MP 462026, India

² NIMS Institute of Allied Medical Sciences and Technology, NIMS University, Jaipur, Rajasthan 303121, India

³ Academy of Scientific and Innovative Research (AcSIR), Ghaziabad 201002, India

⁴ Department of Microbiology, All India Institute of Medical Sciences, Bhopal, MP 462020, India

Graphical Abstract



Keywords Reduced Graphene oxide silver nanocomposites · Green synthesis · Electrochemical biosensing · Antimicrobial activity

Introduction

Nanoscience and its technological advancements pave the way to a fast-emerging field that helps to produce a variety of different metal nanoparticles (MNPs) influencing all the domains of life and soon will be the next industrial boon [1, 2]. Noble MNPs have received a lot of upsurge in the past 2 decades because of their potential applicability in various fields ranging from biosensing and catalysts to optics, microelectronics, environmental bioremediation, antimicrobial agents, as well as usage in targeted drug delivery, diagnostics, and bioimaging [3–7]. Owing to their exceptional physicochemical characteristics, the nanoparticles' size, shape, and composition play a critical role in determining their wide applications. For instance, MNPs exhibit higher electrical conductivity, surface area, stability, and versatility [8]. In particular, metal nanoparticles have drawn substantial interest due to their high absorption in the visible region because of the group excitation of the free electron. These nanoparticles are commonly synthesized by conventional physical and chemical approaches viz., electrochemical reduction, aqueous/non-aqueous chemical reduction, ultrasonic-assisted reduction, microwave-assisted synthesis, micro-emulsion methods, etc. [9–11].

Although, the synthetic processes produce good shape, size, and crystallinity control but often involve the use of toxic chemicals/reagents (strong reducing agents), organic solvents, and severe physicochemical conditions as capping agents to stabilize the size of the nanoparticles and thus are not environmentally benign and may cause dicey effects in biomedical applications [12]. Consequently, the microbe-mediated biosynthesis and assembly of nanoparticles can be employed for the production of clean, non-toxic, controlled polydispersity, and eco-friendly “green chemistry” methods which are free from the use of toxic chemicals and act as a natural capping agent [13, 14]. When compared to chemical approaches, the biosynthetic process produces safer, cost-competitive, and environmentally friendly nanoparticles rich in bioactive molecules. These bioactive compounds can be used as antioxidants and antimicrobial agents.

Novel microbicides are being developed and antimicrobial metallopharmaceuticals have been gaining prominence, since the emergence of multidrug resistance (MDR) pathogens has become a significant public health issue [15, 16]. Among noble MNPs, the biogenesis of silver nanoparticles (AgNPs) of either a simple or composite nature has shown a broad range of bactericidal and fungicidal activities along with versatility in

coordinating with different ligands and macromolecules in microbial cells [17]. The presence of protein caps on MNPs aids in the stabilization and surface area enhancement more effectively which thereby increases drug binding and absorption in patient cells. AgNPs are anticipated to exhibit higher antibacterial activity over bulk silver metal because of good specific surface area and a good fraction of surface atoms. AgNPs are grabbing significant attention compared to other metal nanoparticles due to their strong absorption in the visible light region [18]. Synthesis of nanomaterials from microbes can be extracellular which is simpler and more economical, in contrast to intracellular synthesis where the ions transported into the cell which utilizes the intracellular enzymes and hence requires certain ultrasonic treatments and additional detergents [19]. The silver nanoparticles' potential has been investigated in recent studies for the fabrication of electrochemical biosensors because of its good surface area, high conductivity, and outstanding binding capacities. However, because of their remarkable surface activity, excellent biocompatibility, and electrical conductivity, a variety of carbon nanomaterials (CNMs), including graphene oxide (GO) and reduced graphene oxide (rGO), have also been explored in biosensing applications [20, 21]. They can be used to develop extremely sensitive immunosensors since their huge surface area and oxygen functional groups favor sufficient attachment of biorecognition components like enzymes and antibodies.

The bacteria used for the biogenesis of MNPs are generally recognized as safe (GRAS) that belong to the lactic acid bacteria (LAB) group. Apart from reducing potential, *Lactobacillus* biomass also plays an important role as stabilizing agent. Several studies reported that the 'AgNPs' incorporated with 'rGO' improve the conductivity of the nanomaterial significantly along with good chemical and physical properties which include high conductivity, better stability, low volatility, good stability, and good adhesive characteristics [22, 23]. Additionally, it enhances the functional groups and prevents the aggregation of the nanomaterial. Motivated by this, the present research work involves the biogenesis of AgNPs and Ag-rGO nanocomposite using *Lactobacillus* biomass. The synthesized nanomaterials were characterized and the electrochemical properties were evaluated by employing cyclic voltammetry (CV), differential pulse voltammetry (DPV), and electrochemical impedance spectroscopy (EIS) techniques. Furthermore, the antimicrobial susceptibility of AgNPs and Ag-rGO nanocomposites was evaluated at three different concentrations against multidrug-resistant Gram -ve (*E. coli*) and Gram +ve (*S. aureus*) bacteria. The environmentally benign approach for the synthesis of nanomaterials in this work led to the production of water-dispersible, cost-effective, high-purity silver, and silver

functionalized reduced graphene oxide nanocomposites which exhibit good electrochemical and antimicrobial properties therefore can be used for antimicrobial and biosensing applications.

Materials and Methods

Chemicals Required

The chemicals used for nanomaterial synthesis were Silver Nitrate (extra-pure, > 99.8%), deionized (DI) water, absolute ethanol, Sodium Phosphate Monobasic Dihydrate ($\text{NaH}_2\text{PO}_4 \cdot 2\text{H}_2\text{O}$, 98.0%), Sodium Phosphate Dibasic Dihydrate ($\text{Na}_2\text{HPO}_4 \cdot 2\text{H}_2\text{O}$, 98.0%), Potassium Chloride (KCl, 99.0%), Potassium Ferricyanide [$\text{K}_3\text{Fe}(\text{CN})_6$, $\geq 99.0\%$], Potassium Ferrocyanide [$\text{K}_4\text{Fe}(\text{CN})_6 \cdot 3\text{H}_2\text{O}$, ACS grade], and Sodium Hydroxide (NaOH, 98.0%). In the above mentioned, the pure analytical grade chemicals were purchased from SRL and used as it is without any additional processing. A modified Hummer's approach was used to synthesize graphene oxide (GO). Graphite powder ($\geq 99.0\%$) was purchased from Sigma-Aldrich, USA [24].

Bacterial Culture Preparation

The fresh curd was taken as a source of *Lactobacillus* spp. The bacterial culture was prepared by autoclaving 125 mL of *Lactobacillus* MRS Broth in an Erlenmeyer flask, allowing it to cool to room temperature (37 °C). Following this, the inoculum was made by mixing 100 μL curd in 900 μL of deionized water and added in the culture broth [14]. After that, the broth is incubated for ~ 12 h at 37 °C under a continuous shaking condition. Following a 24-h period, the culture was diluted four times, and the volume was made up to 500 mL with constant stirring.

Biogenesis of AgNPs and Ag-rGO Nanocomposites

Following the dilution, after ~ 12 h, 2 mL of AgNO_3 solution (1 mM) was added and the mixture was kept overnight at room temperature. The dark environment of the reaction was maintained. Following a 24-h incubation period, the color of flask containing the silver nitrate turns brown from pale yellow, indicating the synthesis of silver nanoparticles (Ag^+ to Ag^0). The plasmon resonance characteristic of silver nanoparticles is responsible for the development of the brown color. The formation of brown color is due to the plasmon resonance property of AgNPs [25]. The reduction of Ag^+ to Ag^0 happens through the nitrate reductase enzyme. These enzymes released in the solution reduce the Ag^+ to

Ag⁰ through capping agents such as proteins [26]. Similarly, Ag-rGO nanocomposites were synthesized. For this 1 mL of ultrasonicated GO solution (0.2 g) and 2 mL of AgNO₃ solution (1 mM) were added to the 125 mL of the culture and incubated overnight. After that, the culture suspension was centrifuged for 10 min at 10,000 rpm several times followed by ethanol washing to get rid of cell debris and impurities. The obtained mixture was air dried at 60 °C in a hot air oven and the material was weighed on a precision electronic balance. The detailed insights into step-by-step processes of the synthesis of AgNPs and silver-reduced graphene oxide-based nanocomposites are illustrated in Fig. 1.

Characterization of AgNPs and Ag-rGO Nanocomposite

The synthesized AgNPs and Ag-rGO nanomaterial were primarily evaluated by taking the UV–visible spectrum with the help of UV–visible spectroscope (Evolution 220 UV–vis Spectrophotometer, ThermoFisher Scientific). Before measurements, the dried nanoparticles were diluted with Milli-Q water (resistivity 18.2 MΩ·cm) in sample aliquots. The absorbance was measured in the range of 180–700 nm. Fourier transform infrared (FTIR) spectroscopy (Nicolet iS50, Thermo Scientific, USA) was employed to study the functional groups of nanoparticles, and spectra were taken in the region of 400 to 3500 cm⁻¹. Raman spectroscopy (IndiRam CTR300, India) was employed to detect vibrational,

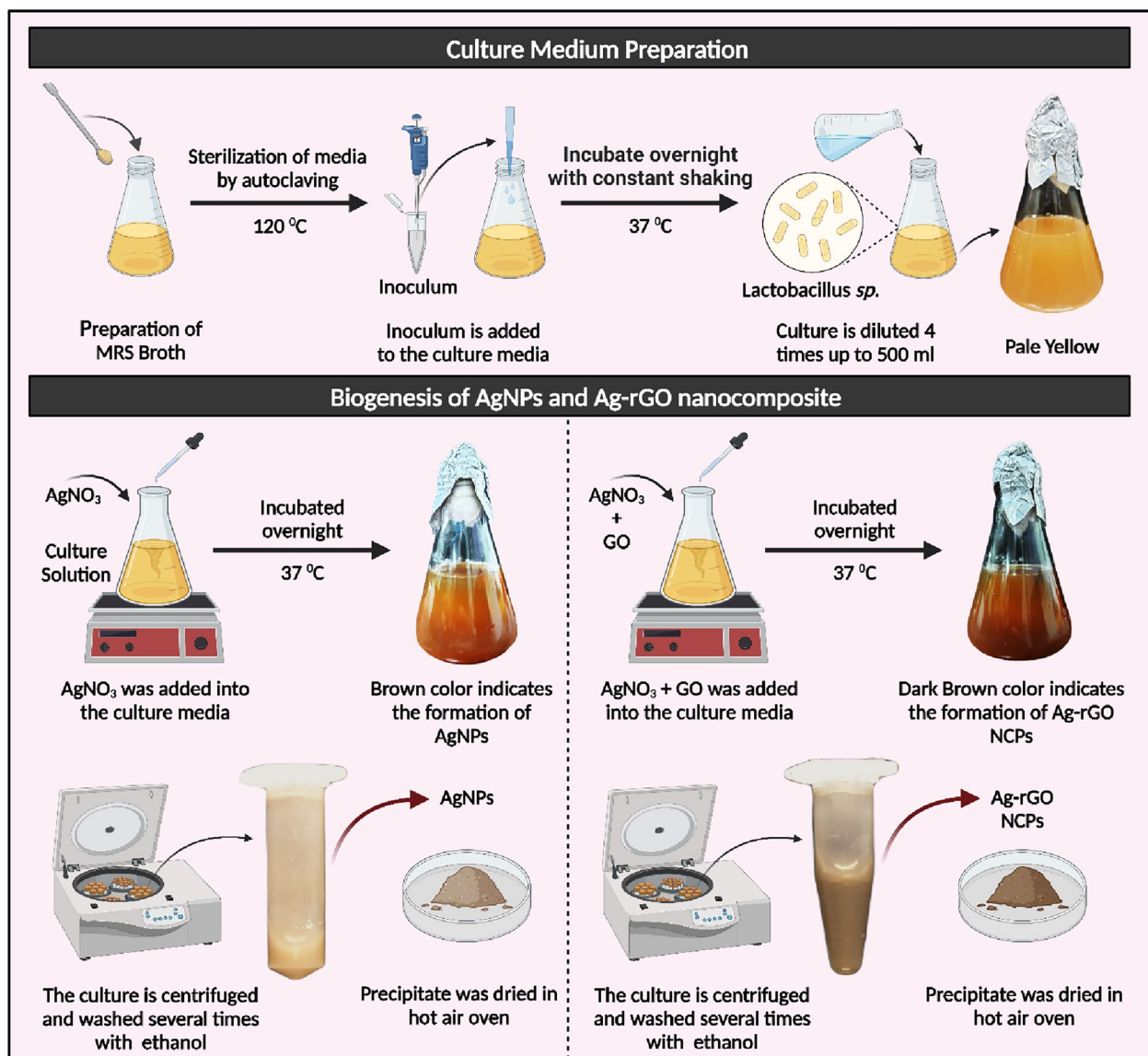


Fig. 1 A diagrammatic representation of the method of culture preparation and biogenesis of AgNPs and Ag-rGO nanocomposite, respectively

rotational, and other states in a molecular signature, capable of probing the chemical constitution of nanomaterials. The crystalline nature of the nanomaterials was confirmed by powder X-ray diffraction method (XRD) (Rigaku Miniflex-1 X-ray diffractometer, $\lambda = 1.5406 \text{ \AA}$, Cu K α radiation). The intensities were recorded from 10° to 80° at 2θ angles. The surface morphology and size of the synthesized nanomaterials were estimated by coating the nanoparticles over sample holder tap-on stubs and observed with the help of Scanning Electron Microscope (ZEISS). The field-emission scanning electron microscopy (FESEM) (FEI Nova NanoSEM 430) was employed to capture the microstructure image of the nanomaterials. The transmission electron microscope (TEM) (JEOL, JEM-F200) was used to take images on the copper grid coated with nanomaterial at 200 keV along with their elemental analysis by Energy Dispersive X-ray spectroscopy (EDX). TEM micrographs were further analyzed to confirm the shape and size of the nanomaterial. The particle size distribution was calculated by measuring the diameters of 100 AgNPs and their nanocomposites using Image J software.

Electrochemical Properties

The electrochemical studies of Ag NPs and Ag-rGO nanocomposite were assessed by employing cyclic voltammetry (CV), differential pulse voltammetry (DPV), and electrochemical impedance spectroscopy (EIS) techniques using a Metrohm Autolab potentiostat/galvanostat workstation (PGSTAT204, the Netherlands) equipped with 3-electrode which include working glassy carbon electrode (GCE) deposited with nanomaterial, platinum (Pt) counter electrode, and an Ag/AgCl in 3 M KCl as a reference electrode. Before experiment, the surface of GCE was extensively cleaned by employing the standard process which involves sonication and washing in 0.1 M H₂SO₄ and 95% ethanol for 2 minutes followed by polishing with first a 0.3 μm α -Al₂O₃ slurry and then a 0.05 μm α -Al₂O₃ slurry. After polishing, GCE was ultrasonicated in distilled water for two minutes to clean the alumina particles and then kept at RT before further use. The 0.1 M phosphate buffer saline (pH 7.4) with 0.1 M KCl and 5 mM ferri/ferrocyanide solution was used for all the experiments also referred to as “redox electrolyte.” CV study was done using -0.3 to 0.8 V potential range at a scan rate of 0.02 Vs^{-1} in a redox electrolyte solution. The DPV study was conducted using -0.3 to 0.8 V potential range with a scan rate $\sim 0.02 \text{ Vs}^{-1}$ and step of 0.01 V. EIS in galvanostat mode was done using 10^5 to 0.1 Hz. Frequency range.

Antimicrobial Assay

The antimicrobial activity of biogenic AgNPs and Ag-rGO nanocomposite was assessed by disk diffusion assay against

pathogenic bacteria such as *Staphylococcus aureus* ATCC 259213 (*S. aureus*) and *Escherichia coli* ATCC 25922 (*E. coli*) on Mueller–Hinton (MH) agar plates which were conducted in the department of microbiology, AIIMS, Bhopal, India. The agar plates were made using a necessary quantity of agar medium and sterilized at 121°C and 15 lbs of pressure in autoclave. Each petri dish was then filled with 25 mL of nutrient agar, which was allowed to dry for 24 h at 37°C in the incubator. To ensure that every region was covered, the bacterial cultures were swabbed equally. The method consists of placing paper discs saturated with nanomaterials on a lawn of bacteria seeded on the agar medium surface followed by incubation of the plate overnight (18 h). Afterward, the presence or absence of a zone of inhibition around the discs was measured [27]. The sterile disk was procured from HIMEDIA SD067-1VL. The different concentrations of AgNPs and Ag-rGO nanocomposites ranging from 1.0, 5.0, and 10.0 mg/ml were used for the assessment of antimicrobial susceptibility assay (AST). The nanomaterial solution was ultrasonicated for 15 min which allow particles to be dispersed evenly before placing them on a disk. All experiments were conducted according to the Clinical and Laboratory Standards Institute (CLSI) norms. While performing experiments, Cefepime (CPM 30) and Doxycycline (DO 30) were used as the control antibiotic against respective microorganisms. Each set of experiments has been repeated thrice.

Results and Discussions

The green synthesized Ag NPs and Ag-rGO nanomaterial were characterized and analyzed by various techniques. They were characterized using UV–vis, FTIR, XRD, Raman spectroscopy, FESEM, TEM, and EDX techniques. Additionally, the electrochemical properties were also evaluated using CV, DPV, and EIS, respectively. The results revealed the chemical and surface properties of the Ag NPs and Ag-rGO nanocomposite for effective use in the biomedical field.

Characterization of AgNPs/rGO Nanocomposites

Before their electrochemical characterization, the synthesized AgNPs and Ag-rGO nanocomposites were evaluated for their structural, optical, and morphological properties. Optical properties were studied using a UV–visible spectroscopy, which primarily confirmed the successful synthesis as shown in Fig. 2A. The free electrons in metal nanoparticles generate a surface plasmon resonance (SPR) band, due to the mutual vibration of electrons of nanomaterial upon exposure to light waves [28]. The appearances of the peaks show the SPR properties of silver nanoparticles. The UV–visible spectra of AgNPs depict strong peaks at 420–450 nm wavelengths. The absorption band at 265 nm may be due

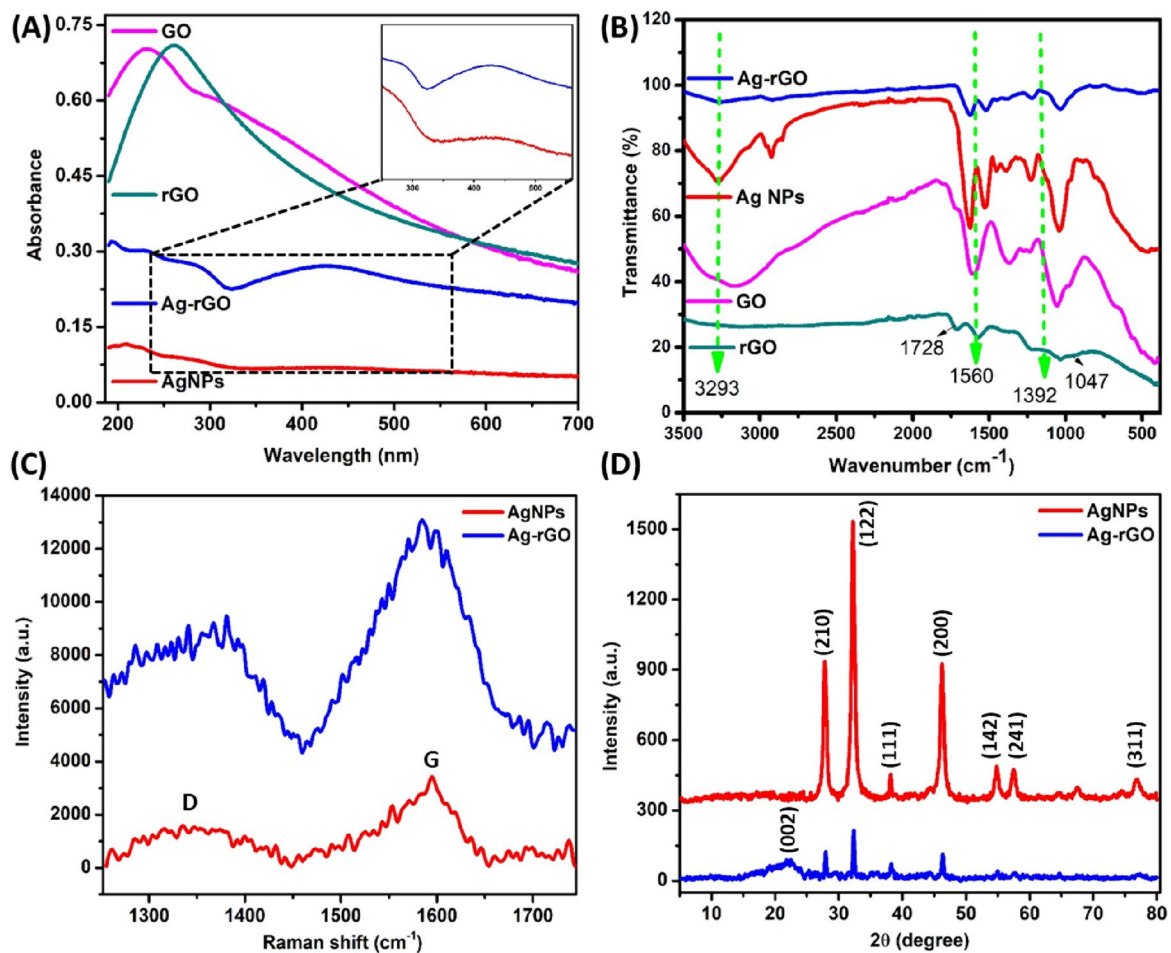


Fig. 2 **A** UV–visible curve of GO, rGO, AgNPs & Ag-rGO (insets show characteristics peak at 435 and 430 nm for AgNPs and Ag-rGO, respectively). **B** FTIR curve of GO, AgNPs & Ag-rGO. **C** Raman curve of AgNPs & Ag-rGO. **D** XRD spectra of AgNPs and Ag-rGO

to bacterial phenols, flavonoids, alkaloids, aromatic amino acids, etc. [29]. Das and group have reported extracellular biosynthesis of AgNPs by a bacterial strain (CS₁₁) which showed a peak at 450 nm in the UV–vis spectrum [30]. Moreover, the Ag-rGO nanocomposite shows three peaks at 213 nm, 267 nm, and 430 nm wavelengths. Nevertheless, the wide peak present between 350 and 500 nm resembles the transitions in high-density part indicating the presence of stable nanoparticles. The frequency and bandwidth of SPR depend on the shape and size of the nanomaterial and also on the dielectric constant of the metal used and the respective medium. Gurunathan and group have reported a non-toxic, simple, environmentally friendly approach for Ag-rGO nanocomposite synthesis using *Tilia amurensis* plant extracts which act as stabilizing and reducing agents which showed a peak at 410 nm in the uv–vis spectrum. They reported the peak of GO at 231 nm and rGO at 261 nm, respectively. The curve of GO exhibits peaks at 237 and 300 nm which are attributed to aromatic C=C bond mediated

π – n transitions and C=O bond mediated n – π transitions of rGO at 262 nm, respectively.

FTIR spectroscopy was used to characterize and estimate the presence of functional groups in the AgNPs/rGO nanocomposites, and it also helps to dictate the secondary structure formed due to nanomaterial–protein interaction. As presented in Fig. 2B, the FTIR curve shows absorption bands at 3269, 2922, 2849, 1632, 1383, 1245, 1032, and 746 cm⁻¹ indicating the presence of a capping agent with the nanomaterials. The observed intense bands were in concordance with the standard values reported in the literature. Kumar and group have reported the characteristic bands of GO, rGO, and Ag@rGO which are attributed to the intercalation of AgNPs between the graphitic sheets of rGO [31]. The highly intense transmittance spectra at 3269 cm⁻¹ are because of the –OH stretching vibrations (asymmetric and symmetric) of the capsular polysaccharides (hydrated molecules) and –NH stretching vibrations because of primary and secondary amines [32]. The bands around 2922 and 1383 cm⁻¹ indicate –CH₂ asymmetrical stretching of

alkenes. These results indicated the presence of proteins that lead to stabilization and inhibit aggregation of nanomaterials. The results confirmed that amino acids and peptides form a stable coat around the nanoparticles. The peak at 1632 cm^{-1} attributed due to amides -NH stretching in the peptide bond and C=C stretching that may also help in nanoparticles stabilization [33]. The results show the presence of absorption bands at 1245 cm^{-1} represents the stretching modes of the epoxide group (C-O-C), while the band at 1032 cm^{-1} because of the vibration of the -CO group [34]. The FTIR data showed that the GO has been exfoliated successfully, and there are good interactions between the functional groups of the rGO sheets surface and AgNPs. The observed peaks of amino acids indicate the protein presence in the filtrate.

Raman spectroscopy is an effective technique for examining lattice distortion or flaws in the structural composition of nanomaterials. The Raman data of AgNPs and their nanocomposite are shown in Fig. 2C. The peaks at 1365 and 1595 cm^{-1} are attributed to the presence of D and G bands, respectively, which indicate the lattice distortion of sp^3 carbon and vibration of sp^2 (C=C). The D-band is linked to the extent of disorder, while the G-band denotes the relative degree of graphitization [35]. Further, a slight shift in the G-band of Ag-rGO nanocomposite has been observed from 1595 to 1590 cm^{-1} , indicating the sp^2 domain recovery. Moreover, the Raman signals of Ag-rGO nanocomposite are stronger than that of AgNPs, respectively. The high-intensity peak usually indicates an increase in specific vibration contributed by a part of that nanomaterial in the sample. Both the intensities (I_D and I_G) bands significantly increased for the Ag-rGO nanocomposite that indicate surface-enhanced Raman scattering (SERS) phenomenon, indicating that the deposition of AgNPs on rGO sheets was successful [36]. Haldorai and group have successfully synthesized Ag@graphene oxide nanocomposite exhibiting 2 strong peaks

approximately at 1359 and 1593 cm^{-1} which denotes the D and G bands, respectively [37].

The crystalline structure analysis of AgNPs and Ag-rGO was done by using X-Ray diffractometer (XRD) as shown in Fig. 2D. The diffraction pattern was obtained at 2θ values ranging from ($10^\circ \leq 2\theta \leq 80^\circ$). The significant diffraction pattern were observed at 27.80° , 32.22° , 38.12° , 46.24° , 54.82° , 57.52° , and 76.96° which are indexed to (210), (122), (111), (200), (142), (241), and (311) planes of pure Ag based on the face-centered cubic structure (JCPDS, file No. 04-0783), respectively. A broad peak is located at 23.5° characteristic of the rGO (002) crystalline plane of the hexagonal shape [38], equivalent to an interlayer distance of 0.34 nm . The XRD data showed that the synthesized AgNPs are crystalline in nature. The size of AgNPs was estimated by using Debye-Scherrer's equation: $D = 0.9\lambda/\beta\cos\theta$, where D is the normal crystallite domain size vertical to the reflecting planes, λ is the wavelength of X-ray, β is the full width at half maximum (FWHM) of the diffraction peak, and θ is the Bragg's angle [39]. The average calculated size is 11.72 nm from the peaks of FWHM. Using Bragg's equation, $2d\sin\theta = n\lambda$, the interplanar spacing was determined. Where, n is order of diffraction (here 1), λ is wavelength of Cu $K\alpha$ X-rays (0.15406 nm or 1.54 \AA), and d is the interplanar space. The estimated interplanar spacing for the following characteristic planes (210), (122), (111), (200), (142), (241), and (311) are 0.32 , 0.28 , 0.24 , 0.20 , 0.17 , 0.16 , and 0.12 nm , respectively. Mickymaray has successfully exhibited three intense peaks at 2θ angles 44.27 , 38.11 , and 77.47° equivalent to (111), (200), and (311) planes, respectively [33].

The FESEM analysis is performed at an accelerating voltage of 15 kV to study silver nanoparticles' surface morphology, microstructure, and surface appearance. It demonstrates that the particles are mainly spherical and aggregate into larger particles refraining from having a distinct morphology. The presence of secondary

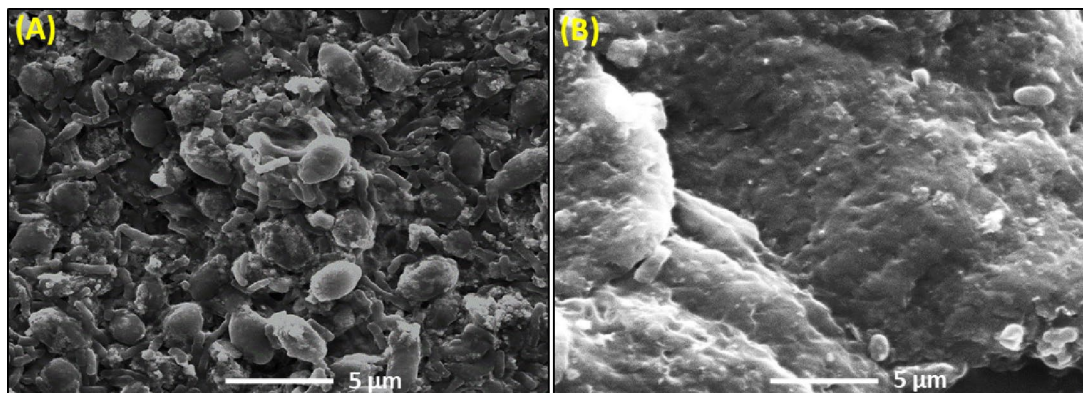


Fig. 3 FESEM images of **A** AgNPs and **B** Ag-rGO nanocomposites at a scale bar of $5\text{ }\mu\text{m}$

metabolites could be the cause of this aggregation. The agglomeration of particles leads to the destabilization of nanoparticles. Proteins play a significant role as capping agents for nanomaterials inhibiting agglomeration thereby providing the nanoparticles stability and a particular structure [40]. The FESEM images clearly show the presence of synthesized AgNPs and Ag-rGO as revealed in Fig. 3. The surface morphology of nanomaterials was oval and spherical. Further, Fig. 3B shows that AgNPs are uniformly decorated on rGO sheets.

The size and structure of the synthesized AgNPs/rGO nanocomposites, which dictate their physical and chemical properties, were examined using TEM. Images obtained by TEM and HRTEM micrographs at different resolutions revealed monodispersed, approximately spherical forms of various sizes ranging from 10 to 30 nm as revealed in Fig. 4. A scrolling edge and wrinkled regions could be seen in the Ag-rGO TEM image in Fig. 4E–G, due to the intrinsic microscopic roughening of graphene sheets. On the rGO sheet surface, there are uniformly decorated with spherical AgNPs with diameter of around 18 nm. The AgNPs aggregate if left unprotected often results in a greatly reduced surface area [41]. The oxygen-containing functionalities on the surface of GO provide the chemically active centers for the attachment of Ag. The FESEM and TEM images showed that AgNPs attached on both sides of GO sheets. On the rGO sheets, AgNPs are dispersed randomly and are not clumped

together. Widely dispersed AgNPs have more surface area and hence worthwhile to increase the catalytic performance [42]. Figure 4D displays the selected area electron diffraction (SAED) data of AgNPs which depict the well-defined, spotty rings, suggesting that the nanoparticles were semi-crystalline, and thus, well aligned with the XRD results. The appearance of concentric rings and distinct spots indicates that the Ag-rGO nanocomposite is polycrystalline, as indicated in Fig. 4H.

Additionally, element mapping was done using EDX spectroscopy to elucidate the distribution of AgNPs/rGO nanocomposite. The characteristic peaks related to the silver are located between 2.5 and 3.5 keV. Kaviya and group demonstrated that metallic Ag nanocrystals exhibit a typical absorption peak due to SPR approximately at 3 keV [43]. The curve plotted between energy (3 keV) and counts displayed strong signals of Ag (36.4 wt%), C (31.5 wt%), Cu (20.4 wt%), and small traces of Cl, Au, and O indicating the successful synthesis of AgNPs as shown in Fig. 5E. In addition, the presence of intensive absorption of Ag (53.5 wt%), C (28.7 wt%), Cu (13.3 wt%), and significant traces of O and Si further confirmed the presence of AgNPs on rGO as shown in Fig. 5J. Weak 'O' signals result from X-ray emissions from proteins, enzymes, and carbohydrates present therein. The high-angle annular dark field-scanning transmission electron microscopy (HAADF-STEM) and analysis of TEM-EDS mapping of a

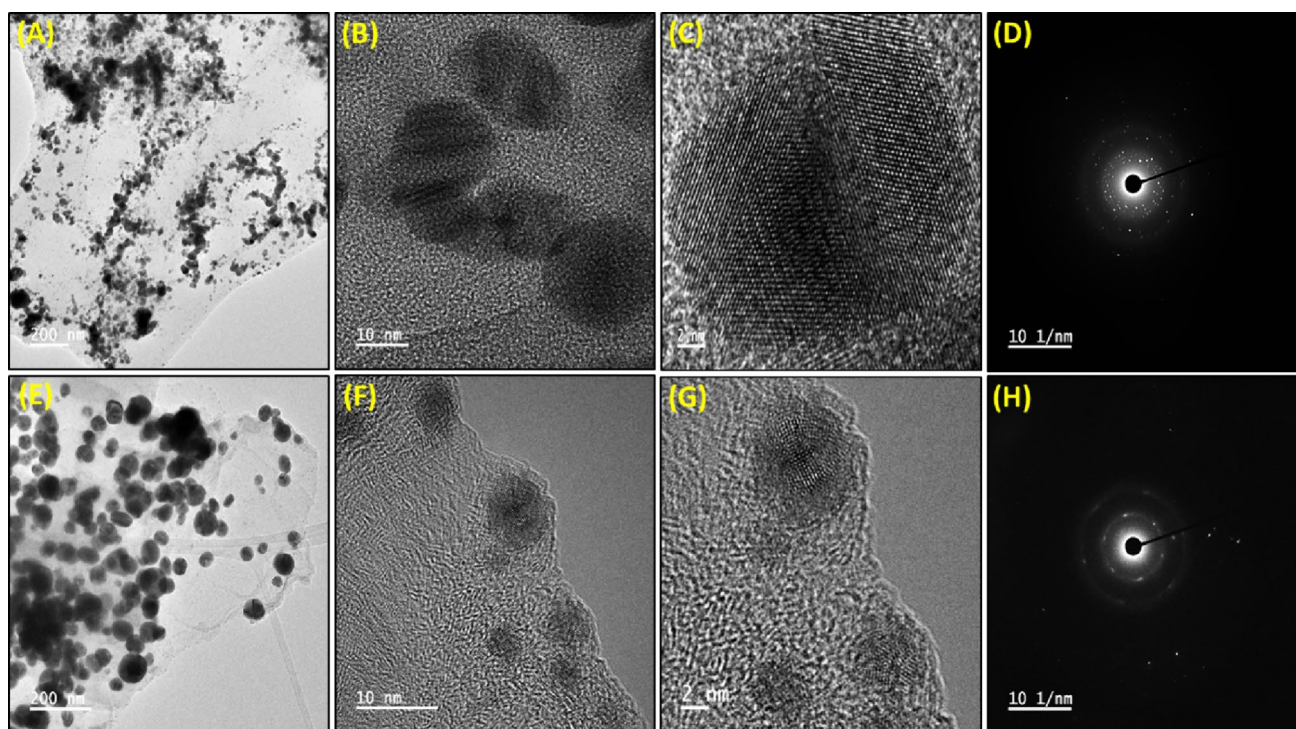


Fig. 4 TEM pictures of AgNPs (A, B) and Ag-rGO (E, F) nanocomposite at 200 and 10 nm scale bar, C, G HRTEM images at 2 nm scale bar, and D, H SAED pattern of AgNPs and Ag-rGO respectively

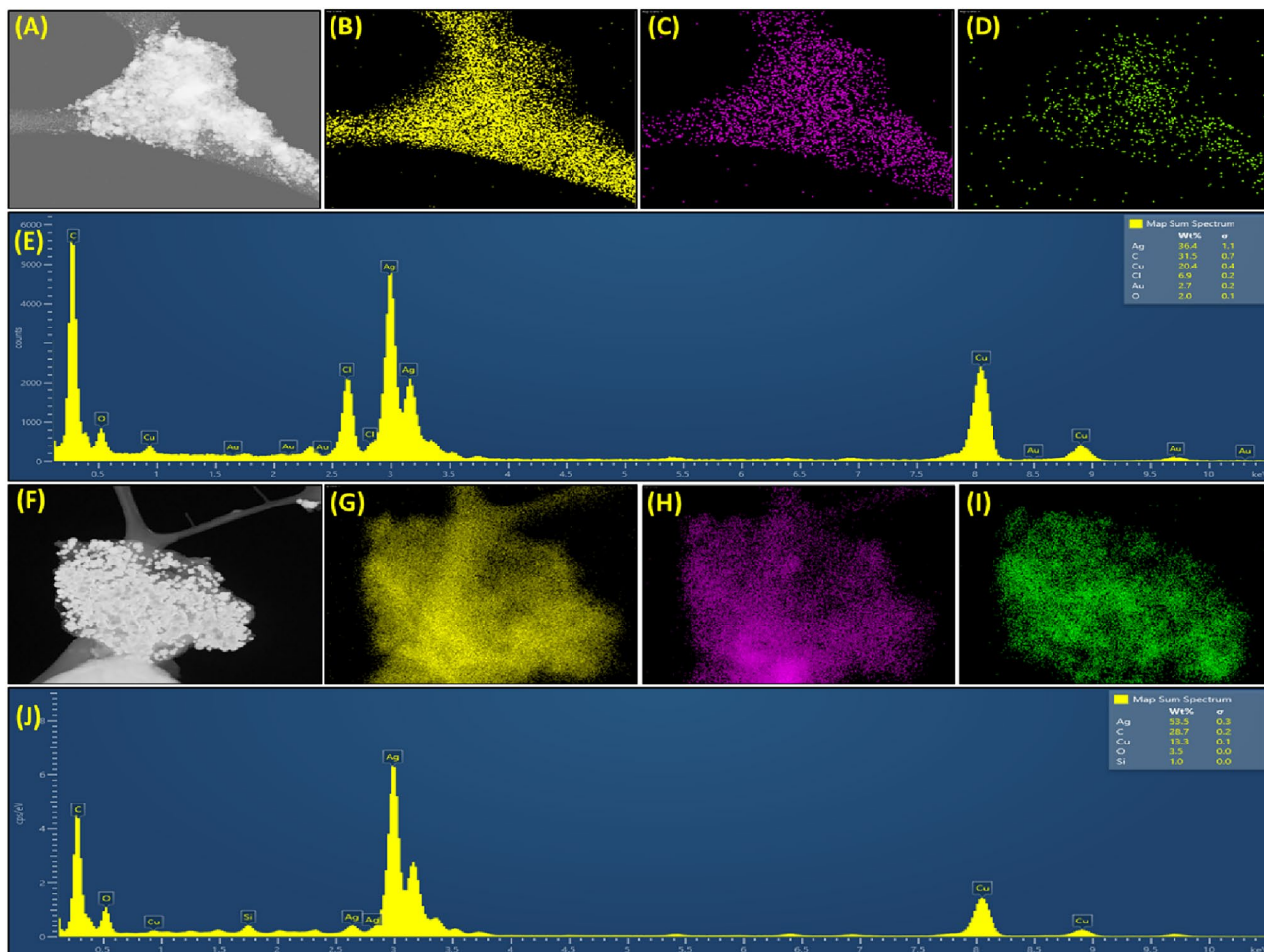


Fig. 5 HAADF-STEM images and Elemental mapping of AgNPs A–E and Ag-rGO F–J nanocomposite, respectively

random site indicate the chemical signatures are uniformly distributed in the nanocomposite as shown in Fig. 5A–D, F–I. Nguyen and group, as well as Li and group, show the peaks of C, N, and O at 285, 400, and 531 eV, respectively, and 3 prominent peaks at 2.99, 3.17, and 3.20 keV which suggest the successful deposition of AgNPs on rGO [44, 45]. There was not a peak that can be used to identify the impurity across the whole scanning range of binding energies. The results obtained confirmed that the product included a highly pure AgNPs/rGO nanocomposite.

While FESEM, TEM, and EDX analyses provide valuable insights into the morphology and elemental composition of the materials, they also elucidate the structure–property relationships of nanomaterials based on the observed structural features with the properties of the materials. For instance, these techniques could discuss how the size and shape of the particles influence the material's properties. Similarly, the elemental composition obtained from EDX could be related to the material's performance. The size of AgNPs is between 10 and

30 nm, while Ag-rGO nanocomposite is ~ 18 nm which indicate that due to smaller size they can be easily penetrated to microbial surface. The EDX results showed that while AgNPs consist of major silver content, the Ag-rGO besides silver also contains carbon and oxygen in higher ratio which could help in stabilization of the nanocomposite and enhance their antimicrobial and electrochemical properties [14].

Electrochemical Analysis

The electrochemical investigation of surface-modified working electrodes (i.e., AgNPs and Ag-rGO nanocomposites) in each step has been performed using electroanalytical techniques such as CV, DPV, and EIS, respectively [46]. All electrochemical analyses were carried out in redox electrolyte.

CV is employed to see the oxidation and reduction of chemical species which showed anodic and cathodic peak current (I_{pa} and I_{pc}) and potential (E_{pa} and E_{pc}), respectively

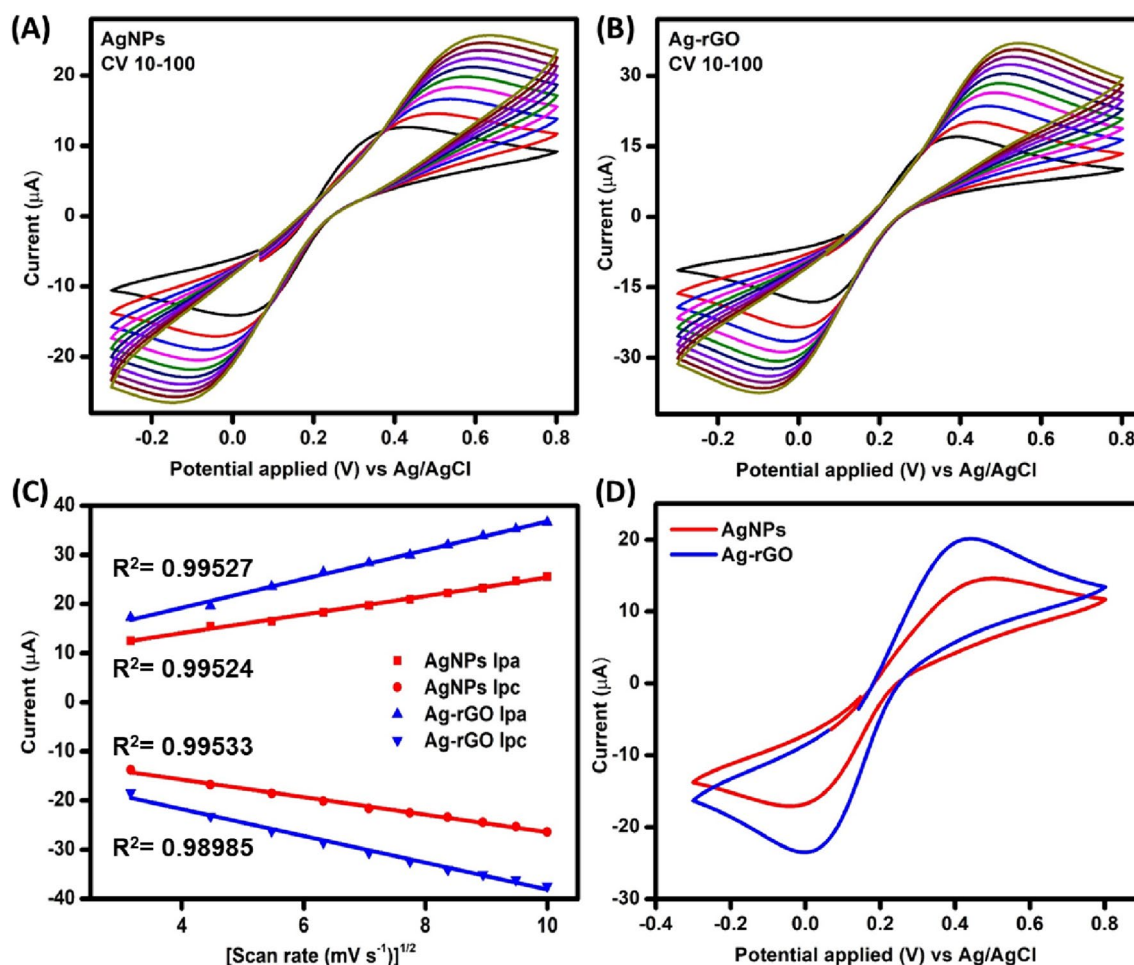


Fig. 6 CV plot from 10 mV s^{-1} to 100 mV s^{-1} . **A** AgNPs, **B** Ag-rGO nanocomposite, **C** Graph of square root of scan rate vs current, and **D** Comparative electrochemical characterization viz., CV of AgNPs and Ag-rGO nanocomposite at 20 mV s^{-1} scan rate, respectively

[47]. The transfer of electrons and the resistance at the electrolyte and working electrode interface are both responsible for variations in peak response. For AgNPs/rGO nanocomposites, as seen in Fig. 6A, B, the peak current increases with the increase in scan rate (from 10 mV s^{-1} to 100 mV s^{-1}). This occurs as a result of the analytes' greater mass transfer to the surface of electrode at higher scan rates. Additionally, the peak currents and potentials of curve showing good conductivity of electrode modified with Ag-rGO nanocomposites (Ag-rGO/GCE, $I_{pa} = 20.02 \text{ } \mu\text{A}$) were significantly higher compared with that of the Ag nanoparticles (AgNPs/GCE, $I_{pa} = 14.22 \text{ } \mu\text{A}$), indicating nanocomposites' increased electrocatalytic activity which suggests that the rGO enhances the electrical conductivity of the Ag which may be due to the enhanced surface area. Roy and group demonstrated that the electroconductivity of Ag-rGO gradually increases concerning GO and rGO alone. Comparing the current from the RGO and RGO/Ag nanomaterial to the GO samples, they are nearly orders of magnitude higher [48]. Another study by Bansal and group showed that the Ag/

rGO nanomaterial has a higher integrated capacitive area than rGO as revealed by CV curves of both nanomaterials at a constant scan rate of 5 mV s^{-1} [49]. The effective surface area (A) of the electrodes was computed by employing the Randles–Sevcik formula, which anticipates that mass transportation occurs merely through diffusion [50]. The A of nanomaterial-deposited electrodes is directly related to the peak currents. The equation describes the effect of the scan rate on the peak current (I_p).

$$I_p = 2.69 \times 10^5 n^{3/2} AC \sqrt{Dv} \quad (1)$$

where I_p = current maximum in amps, the constant with a value of 2.69×10^5 has units in $\text{C mol}^{-1} \text{ V}^{-1/2}$, n = no. of electrons transported in the redox event (usually 1), A = surface area of the electrode in cm^2 (the diameter is 0.3 cm, and the geometrical surface area is 0.07 cm^2), C = concentration of the redox electrolyte solution in mol/cm^3 (here, $5 \times 10^{-6} \text{ mol cm}^{-3}$), D = diffusion coefficient of the redox

electrolyte in cm^2/s (here, $7.26 \times 10^{-6} \text{ cm}^2 \text{ s}^{-1}$), and ν = scan rate in V/s (here, 0.02 Vs^{-1}).

To comprehend the effects of anodic (I_{pa}) and cathodic (I_{pc}) peak currents on the electrode, the significance of the scan rate (ν) was reviewed. The scan rate of the modified electrodes regulates electron transfer redox and diffusion control mechanism. The graph of peak current ν vs the square root of the scan rate revealed linear relation at the potential difference of -0.3 V to 0.8 V in the scan rate range from 10 mV/s to 100 mV/s at the interval of 10 mV/s , as seen in Fig. 6C. The values of anodic peak currents (I_{pa}) enhanced with the scan rate increase and those of cathodic peak currents (I_{pc}) reduce with the increase in scan rate, revealing diffusion-controlled reaction and reversible electron transfer kinetics. Higher current responses resulted from the decreasing electrode's diffusion layer due to the increasing scan rate. The relationship between anodic (I_{pa}) and cathodic peak currents (I_{pc}) ν vs square root of scan rate ($\nu^{1/2}$) were compared using regression curves. It was found to be linear for the AgNPs/GCE and Ag-rGO/GCE and are represented as follows:

$$\begin{aligned} I_{pa}(\text{Ag-rGO/GCE})(\mu\text{A}) \\ = 7.518\nu^{(1/2)}(\text{Vs} - 1) + 2.931, R^2 \\ = 0.99533 \end{aligned} \quad (2)$$

$$\begin{aligned} I_{pc}(\text{Ag-rGO/GCE})(\mu\text{A}) \\ = -10.859\nu^{(1/2)}(\text{Vs} - 1) - 2.725, R^2 \\ = 0.98985 \end{aligned} \quad (3)$$

$$\begin{aligned} I_{pa}(\text{AgNPs/GCE})(\mu\text{A}) \\ = 6.551\nu^{(1/2)}(\text{Vs} - 1) + 1.884, R^2 = 0.99527 \end{aligned} \quad (4)$$

$$\begin{aligned} I_{pc}(\text{AgNPs/GCE})(\mu\text{A}) \\ = -8.620\nu^{(1/2)}(\text{Vs} - 1) - 1.783, R^2 = 0.99524 \end{aligned} \quad (5)$$

The relationship exhibits good linearity, which is substantiated by the values of the corresponding regression coefficients (R^2). A comparative cyclic voltammogram is plotted for AgNPs/rGO nanocomposites at 20 mV s^{-1} scan rate as depicted in Fig. 6D, owing to its excellent biosensing properties.

DPV is an ultrasensitive analytical technique employed to estimate the current response of surface-modified electrodes. The quantitative detection of target analytes is made possible directly by the linear calibration curve of the signal response with respect to the target analyte concentration. The obtained DPV curve at a scan rate of 20 mV s^{-1} of Ag-rGO nanomaterial exhibits a higher peak current than AgNPs, showing its higher electrical conductivity. The peak

current showed that the conductivity of GCE modified with Ag-rGO nanocomposites (Ag-rGO/GCE) was $6.78 \mu\text{A}$ and that for nanoparticles (AgNPs/GCE) was $3.81 \mu\text{A}$, respectively, as shown in Fig. 7A. The results obtained from DPV experiments were in concordance with the CV studies.

EIS was used to study the modified electrode interfacial properties which were reflected by the measurement of charge transfer resistance (R_{ct}) of the AgNPs/GCE, and Ag-rGO/GCE in the frequency range from 0.1 to 10^5 Hz . A Nyquist plot in Fig. 7B showed the semicircle denoted the electrode R_{ct} values. Higher impedance values on the right side of the curve correlate to low-frequency data, whereas lower impedance values on the left part of the plot correspond to higher-frequency region [51]. The charge transfer resistance (R_{ct}) generally known as the semicircle section of the Nyquist graph generated at a high-frequency range reveals the ability of the electrode to transport electrons from the electrode surface to the redox electrolyte solution. The linear part of the graph at the low-frequency part suggests the diffusion-controlled nature at the electrode, that dictates the time of reaction. From the Nyquist plot, as shown in Fig. 7B, GCE modified with Ag-rGO nanocomposites has lower R_{ct} values, i.e., 2250.0Ω (smaller semicircle) compared to the AgNPs' higher R_{ct} values, i.e., 3350.0Ω (larger semicircle) suggesting higher charge transfer activity of the nanocomposites (i.e., lower the R_{ct} values, the higher will be the electroconductivity). In addition, the Bode plot in Fig. 7C, D shows the correlation between frequency ν vs logarithm of the impedance Z (Ω) and phase shift (in degree). The Bode format minimized the data scattering and indicates the electrochemical nature in low-frequency values ($\sim 1000 \text{ Hz}$), whereas in high-frequency regions ($> 1000 \text{ Hz}$) the solution resistance on the Bode plot resembles to a plateau with a phase angle of 0° . Increases in phase angles up to 70 degrees were utilized to categorize the median frequencies ($1000\text{--}10 \text{ Hz}$) and ascertain the capacitive behavior of electrode, specifying the dielectric properties of conductive electrode interface. Mass transfer processes, electron charge transfer properties, and other relaxation actions arose at the edge between the redox solution and electrode at frequencies less than 10 Hz .

Antimicrobial Assessment

The antimicrobial assay is a crucial technique for determining the inhibitory spectra of myriad compounds by testing and screening their effects against pathogenic microorganisms [52]. In this work, the antibacterial activity of the bio-synthesized AgNPs/rGO nanocomposites against multidrug-resistant pathogenic bacteria such as *E. coli* (Gram -ve), and *S. aureus* (Gram + ve) in three different concentrations (1.0 , 5.0 , and 10.0 mg/mL) was carried out by the disk diffusion

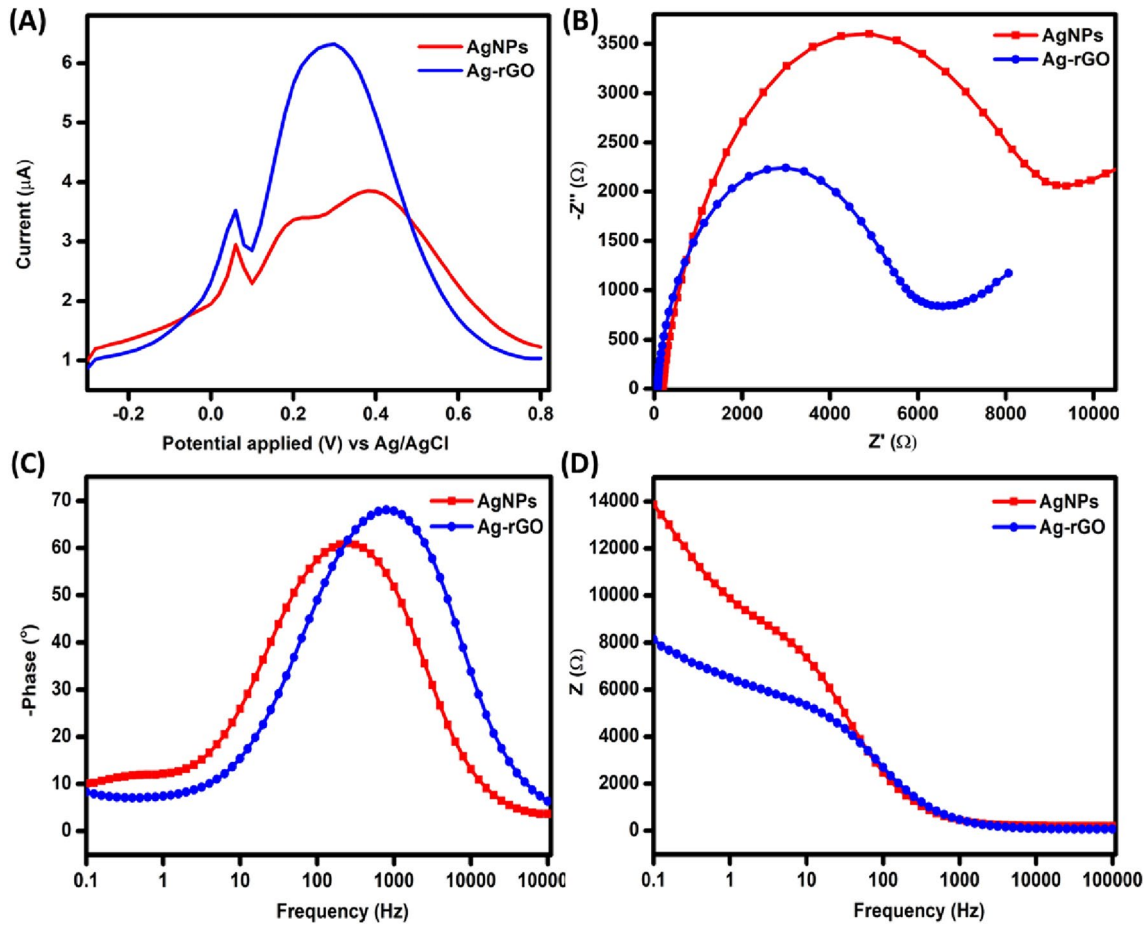
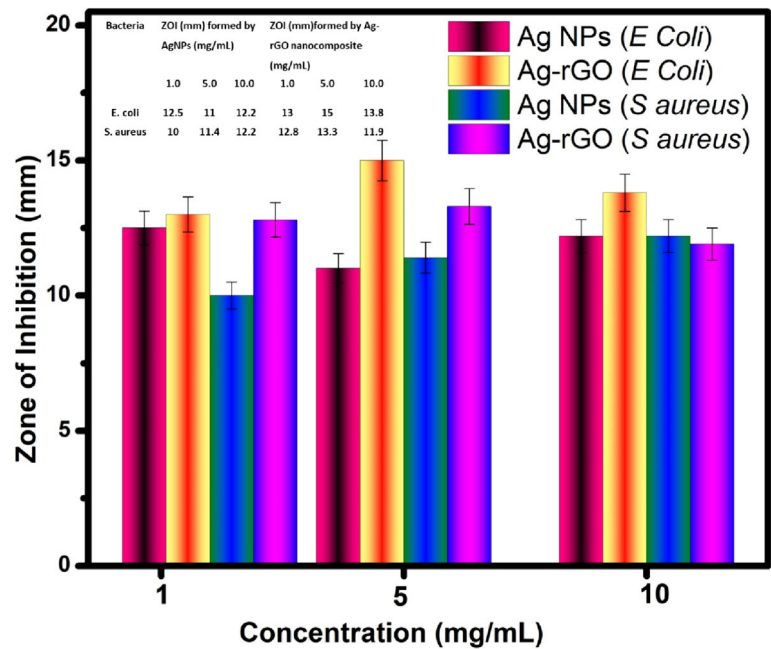


Fig. 7 A Comparative electrochemical characterization via DPV at 20 mV s^{-1} scan rate, B Nyquist plot, and C, D Bode plots of AgNPs and Ag-rGO nanocomposite, respectively

Fig. 8 Zone of inhibition vs concentrations of AgNPs and Ag-rGO nanocomposites plot

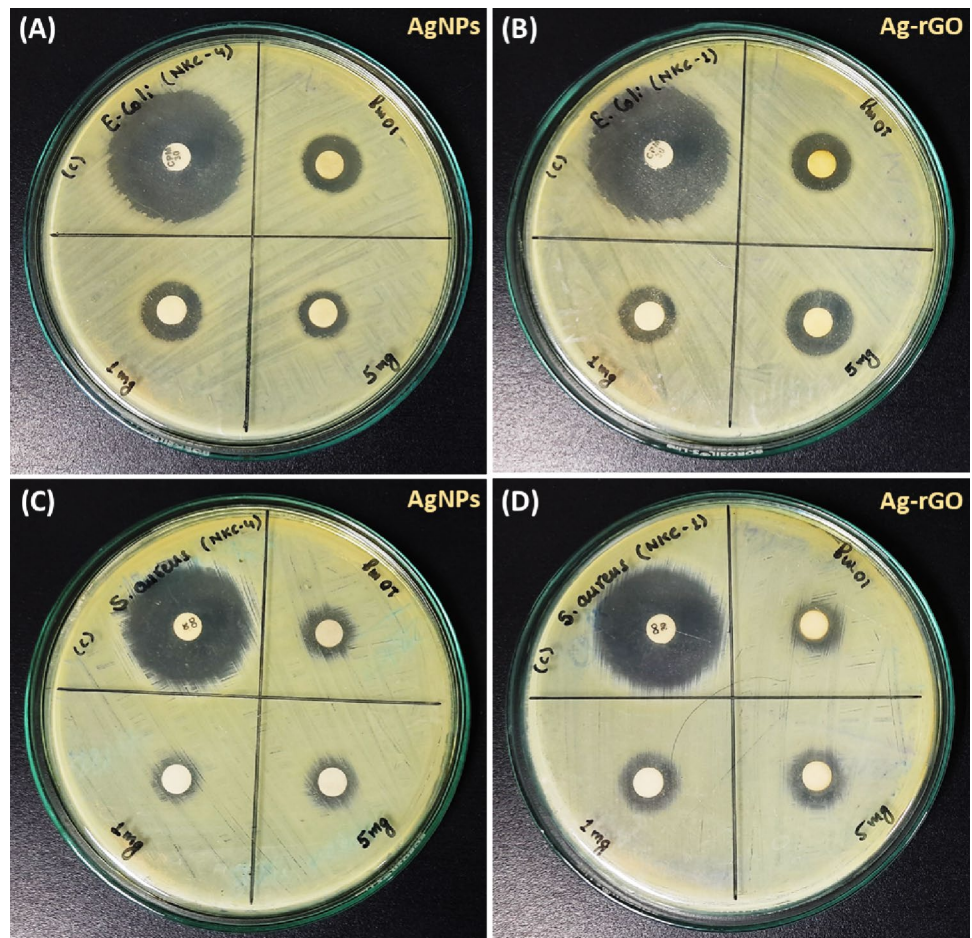


method. Because of high surface area-to-volume ratio, silver nanoparticles show significant antibacterial activity [53]. Also, bacteria contain sulfur and phosphorus compounds and that silver has a higher affinity for reacting with these chemicals, bacterial membrane proteins, and DNA serves as preferred sites for the interaction of AgNPs by electrostatic attraction [54]. Besides, rGO displays several antimicrobial activity because of its ability to disrupt cell membrane of bacteria and induce oxidative stress against a set of pathogens [55]. The bactericidal effect of Ag^+ and the membrane-disrupting effect of the polymer subunits in AgNPs obeyed a dual-action mechanism of antibacterial activity. The plot of zone of inhibition (ZOI) vs different concentration of nanomaterial is shown in Fig. 8. The ZOI surrounding the disk is designated as a function of inhibition of growth due to the antimicrobial activity of AgNPs and Ag-rGO nanocomposites as shown in Fig. 9. The ZOI for Ag-rGO was consistently higher than that of AgNPs for both bacteria suggesting that nanocomposites have excellent antimicrobial activity and the data are tabulated in inset of Fig. 8. The results revealed that the size of the zone of inhibition (ZOI) increases when the concentration of nanomaterial increases from 1 to 5 mg/mL. However, when we further increased the

concentration to 10 mg/mL, the size of ZOI either remained the same or slightly decreased. This may happen due to the aggregation of nanomaterial in higher concentrations which hinders its uptake by the bacterial cell membrane.

Furthermore, Gram -ve bacteria exhibit a greater ZOI than Gram +ve bacteria due to variations in the cell wall composition of both bacteria. In Gram +ve bacteria, the cell wall comprises a thick peptidoglycan layer formed by linear chains of N-acetylglucosamine (NAG) and N-acetylmuramic acid (NAM) linked together as compared with a thin peptidoglycan layer in Gram -ve bacteria making a rigid structure, enhances difficulties in penetration of the AgNPs [56]. Wu and group studied the antibacterial properties against *E. coli* and *S. aureus* bacteria and reported that *E. coli* is much sensitive to the Ag nanomaterial than *S. aureus* because Gram +ve bacteria have thicker membrane than those of the Gram -ve bacteria [57]. AgNPs and Ag-rGO nanocomposites have shown promising antimicrobial properties against *E. coli* and *S. aureus* due to two probable reasons. Firstly, AgNPs can attach to the cell membrane of bacteria and penetrate it, causing structural changes in the cell membrane that lead to cell death. Secondly, AgNPs can generate reactive oxygen species (ROS), which can cause oxidative

Fig. 9 Antimicrobial susceptibility testing of AgNPs and Ag-rGO nanocomposite against multidrug-resistant pathogenic bacteria. **A, B** *E. coli* and **C, D** *S. aureus* in different concentrations (1.0, 5.0, and 10.0 mg/ml)



stress, damage cellular components, and lead to cell death. As for Ag-rGO nanocomposites, they combine the antimicrobial properties of AgNPs with the high surface area and stability of rGO. The rGO can enhance the contact between AgNPs and bacteria, increasing the antimicrobial efficiency. Moreover, the presence of rGO can slow down the release of silver ions, providing a sustained antimicrobial effect [56, 57]. The observed potent antimicrobial activity against the tested bacteria using AgNPs and Ag-rGO nanocomposites can be due to this reason; however, further studies are needed to fully understand the underlying mechanisms and to optimize these nanomaterials for potential applications in antimicrobial therapies. A gradual increase and decrease in the diameter of the ZOI were observed, confirming that the nanoparticles' antimicrobial activity strongly depends on the concentration of nanomaterials. Instead of employing synthetic antibiotics, the study emphasized on using natural metabolites to eradicate MRSA, and this proved to be the most appropriate strategy. The study's noteworthy findings will offer important insights into the management of multidrug-resistant infections. A study by Suresh and group shows that various chemical and biological coatings on nanoparticles have a highly substantial impact on their toxicity, which may be caused by an interaction between the bacteria and the capping agent [58]. Due to their greater surface interaction with bacteria, which is made possible by their biological capping agents, this study demonstrates that biologically synthesized silver nanoparticles have the strongest antibacterial activity. Recently, Barabadi et al. biosynthesized AgNPs using *Pimpinella anisum* seeds. The AgNPs have demonstrated significant antimicrobial efficacy against *E. coli* via reactive oxygen species-mediated mechanism [59]. In this study, we focused on the antimicrobial activity of AgNPs and Ag-rGO nanocomposites. However, we recognize that several variables such as the size, shape, and surface chemistry of nanoparticles could influence antimicrobial efficacy. Smaller nanoparticles have a larger surface area-to-volume ratio, which can enhance their interaction with microbial cells. The shape of nanoparticles can influence their ability to penetrate cell membranes, and the surface chemistry determines the release rate of silver ions and their interaction with microbial cells. While our results are promising, they should be interpreted with consideration of these factors. However, further studies are needed to systematically vary these parameters to fully understand their impact on the antimicrobial activity of nanocomposite.

Conclusion

This study demonstrates the biogenic synthesis of AgNPs and Ag-rGO nanocomposite by employing *Lactobacillus* biomass which acts as a capping, stabilizing, and reducing

agent, produces robust, cost-effective, and high-yielding nanoparticles. The synthesis procedure is environmentally benign and does not involve any use of toxic chemicals or organic solvents. The biologically produced AgNPs and Ag-rGO nanocomposite have been evaluated and characterized using various physicochemical and electrochemical techniques. The structural and morphological analyses revealed that the nanoparticles were face-centered crystals. A wide absorption peak between 350 and 500 nm was visible in the UV-vis spectra, suggesting the presence of stable nanoparticles. The results of the FTIR analysis suggested that the proteins may have been crucial capping agents that stabilized the nanoparticles. TEM examination illustrated that the nanoparticles have spherical shape and ranged in size from 10 to 30 nm. AgNPs were shown to be crystalline by SAED and XRD patterns. Further, CV, DPV, and EIS results showed that the nanocomposite exhibits excellent electrochemical properties which can be utilized to fabricate effective biosensors. The synthesized nanomaterials exhibit good antimicrobial activity against *E. coli* and *S. aureus*. The green synthesis process reported in this work led to the synthesis of water-dispersible, cost-effective, high purity, silver, and reduced graphene oxide silver nanocomposite having good electrochemical and antimicrobial properties. Taken together, the synthesized silver functionalized reduced graphene oxide nanocomposite can be employed in clinical settings and can be effective against pathogenic bacteria.

Acknowledgements The authors would like to thank the director of CSIR-AMPRI for his guidance and encouragement in this project. AP would like to thank DST (DST/WOS-B/HN-4/2021) for fellowship offered under DST WOS-B scheme.

Author Contributions AP conceptualized idea, design experiments, analyze, and interpret results, writing, review, and editing original draft. NKC and PK perform experiments, data acquisition, analysis, and writing original draft. RK supervised work, data analysis, and writing, review, and editing. AG contributed toward antimicrobial efficacy experiments, writing, review, and editing.

Data Availability All data generated or analyzed during this study are included in this published article.

Declarations

Conflict of interest The authors declare that they have no conflict of interest.

References

1. M.T. Yaraki, S. ZahedNasab, I. Zare, M. Dahri, M. MoeinSadeghi, M. Koochi, Y.N. Tan, *Ind. Eng. Chem. Res.* **61**, 7547 (2022)
2. A. Parihar, N.K. Choudhary, P. Sharma, R. Khan, *Environ. Pollut.* **316**, 120695 (2023)
3. B. Kłębowski, J. Depciuch, M. Parlińska-Wojtan, J. Baran, *Int. J. Mol. Sci.* **19**, 4031 (2018)

4. A. Parihar, A. Singhal, N. Kumar, R. Khan, M.A. Khan, A.K. Srivastava, *Nano-Micro Lett.* **14**, 1 (2022)
5. A. Parihar, S. Yadav, M.A. Sadique, P. Ranjan, N. Kumar, A. Singhal, V. Khare, R. Khan, S. Natarajan, A.K. Srivastava, *Bioeng. Transl. Med.* **8**, e10481 (2023)
6. A. Parihar, V. Pandita, R. Khan, *Biotechnol. Bioeng.* **119**, 2669 (2022)
7. A. Parihar, T. Zafar, R. Khandia, D. Singh, P. Barkatullah, R. Dhote, Y. Mishra, *Arch. Proteomics and Bioinformatics* **3** (1) (2022)
8. A. Thakur, S. Kaya, A. Kumar, *Appl. Sci.* **2023**(13), 730 (2023)
9. M. Iordache, A. Oubraham, I.S. Sorlei, F.A. Lungu, C. Capris, T. Popescu, A. Marinouiu, *Nanomaterials* **13**, 1 (2023)
10. A. Parihar and R. Khan, *ACS Appl. Nano Mater.* (2023)
11. A. Parihar, R. Srivastava, A. Dube, *J. Photochem. Photobiol.* **5**, 100013 (2021)
12. S. Iravani, H. Korbekandi, S.V. Mirmohammadi, B. Zolfaghari, *Res. Pharm. Sci.* **9**, 385 (2014)
13. R.K. Das, V.L. Pachapur, L. Lonappan, M. Naghdi, R. Pulicharla, S. Maiti, M. Cledon, L.M.A. Dalila, S.J. Sarma, S.K. Brar, *Nanotechnol. Environ. Eng.* **2**, 1 (2017)
14. A. Parihar, P. Sharma, N. Kumar Choudhary, R. Khan, A. Gupta, R. Kumar Sen, H. Chandra Prasad, M. Ashiq, *ACS Appl. Bio Mater.* **6**, 3706 (2023)
15. M. Bassetti, E. Righi, *Langenbeck's Arch. Surg.* **400**, 153 (2015)
16. A. Parihar, S. S. Ahmed, P. Sharma, N. K. Choudhary, F. Akter, M. A. Ali, Z. F. Sonia, R. Khan, *Mol. Simul.* **49**(12), 1267–1279 (2022)
17. M. Asif, R. Yasmin, R. Asif, A. Ambreen, M. Mustafa, S. Umbreen, *Dose-Response* **20**, 1 (2022)
18. E. Sánchez-López, D. Gomes, G. Esteruelas, L. Bonilla, A.L. Lopez-Machado, R. Galindo, A. Cano, M. Espina, M. Ettcheto, A. Camins, A.M. Silva, A. Durazzo, A. Santini, M.L. Garcia, E.B. Souto, *Nanomater.* **10**, 292 (2020)
19. S. Ghosh, R. Ahmad, M. Zeyauallah, S.K. Khare, *Front. Chem.* **9**, 626834 (2021)
20. D. Chen, H. Feng, J. Li, *Chem. Rev.* **112**, 6027 (2012)
21. A. Parihar, N.K. Choudhary, P. Sharma, R. Khan, *Mater. Today Chem.* **30**, 101499 (2023)
22. S. Bhattacharjee, C.R. Macintyre, X. Wen, P. Bahl, U. Kumar, A.A. Chughtai, R. Joshi, *Carbon NY* **166**, 148 (2020)
23. A.T. Smith, A.M. LaChance, S. Zeng, B. Liu, L. Sun, *Nano Mater. Sci.* **1**, 31 (2019)
24. R. Muzyka, M. Kwoka, Ł. Smeđowski, N. Díez, G. Gryglewicz, *New Carbon Mater.* **32**, 15 (2017)
25. S.I. Rasmagin, L.A. Apresyan, *Opt. Spectrosc.* **128**, 327 (2020)
26. T. Mabey, D. Andrea Cristaldi, P. Oyston, K.P. Lymer, E. Stulz, S. Wilks, C. William Keevil, X. Zhang, *Crit. Rev. Biotech.* **39**, 272 (2019). <https://doi.org/10.1080/07388551.2018.1555130>
27. F.C. Tenover, *Antimicrobial Drug Resistance* (Springer, Chem, 2017), p.1347
28. H. Yu, Y. Peng, Y. Yang, Z.Y. Li, *NPJ Comput. Mater.* **5**, 1 (2019)
29. Y.N. Tan, J.Y. Lee, D.I.C. Wang, *J. Am. Chem. Soc.* **132**, 5677 (2010)
30. V.L. Das, Roshmi, T. Rintu, T. Varghese, E.V. Soniya, J. Mathew, E.K. Radhakrishnan, *3 Biotech* **4**, 121 (2013)
31. A. Kumar, A.M. Sadanandhan, S.L. Jain, *New J. Chem.* **43**, 9116 (2019)
32. M.R. D'Oliveira, J. Rabelo, A.G. Veiga, C.A. Chagas, M. Schmal, *Catal. Letters* **150**, 3036 (2020)
33. S. Mickymaray, *Biomolecules* **9**, 662 (2019)
34. A. Mathkar, D. Tozier, P. Cox, P. Ong, C. Galande, K. Balakrishnan, A. LeelaMohana Reddy, P.M. Ajayan, *J. Phys. Chem. Lett.* **3**, 986 (2012)
35. H. Zhou, C. Qiu, F. Yu, H. Yang, M. Chen, L. Hu, L. Sun, *J. Phys. Chem. C* **115**, 11348 (2011)
36. G. Lu, H. Li, C. Liusman, Z. Yin, S. Wu, H. Zhang, *Chem. Sci.* **2**, 1817 (2011)
37. Y. Haldorai, B.K. Kim, Y.L. Jo, J.J. Shim, *Mater. Chem. Phys.* **143**, 1452 (2014)
38. S. Abdolhosseinzadeh, H. Asgharzadeh, H.S. Kim, *Sci. Reports* **5**, 1 (2015)
39. S. Roy, S. Shankar, J.W. Rhim, *Food Hydrocoll.* **88**, 237 (2019)
40. R. Javed, M. Zia, S. Naz, S.O. Aisida, N. ul Ain, Q. Ao, *J. Nanobiotechnol.* **18**, 1 (2020)
41. P. Béltéky, A. Rónavári, N. Igaz, B. Szerencsés, I.Y. Tóth, I. Pfeiffer, M. Kiricsi, Z. Kónya, *Int. J. Nanomedicine* **14**, 667 (2019)
42. A. Dandia, A. Sharma, V. Parewa, B. Kumawat, K.S. Rathore, *RSC Adv.* **5**, 91888 (2015)
43. S. Kaviya, J. Santhanalakshmi, B. Viswanathan, J. Muthumary, K. Srinivasan, *Spectrochim. Acta Part A* **79**, 594 (2011)
44. N.D. Nguyen, T. Van Nguyen, A.D. Chu, H.V. Tran, L.T. Tran, C.D. Huynh, *Arab. J. Chem.* **11**, 1134 (2018)
45. K. Li, S. Cui, J. Hu, Y. Zhou, Y. Liu, *Carbohydr. Polym.* **199**, 68 (2018)
46. R. Khan, A. Parihar, S. Sanghi (eds.), *Biosensor Based Advanced Cancer Diagnostics: From Lab to Clinics*. Academic Press, USA (2021)
47. N. Elgrishi, K.J. Rountree, B.D. McCarthy, E.S. Rountree, T.T. Eisenhart, J.L. Dempsey, *J. Chem. Educ.* **95**, 197 (2018)
48. I. Roy, D. Rana, G. Sarkar, A. Bhattacharyya, N.R. Saha, S. Mondal, S. Pattanayak, S. Chattopadhyay, D. Chattopadhyay, *RSC Adv.* **5**, 25357 (2015)
49. K. Bansal, J. Singh, A.S. Dhaliwal, *Fullerenes Nanotubes Carbon Nanostruct.* **31**, 277 (2022). <https://doi.org/10.1080/1536383X.2022.2144840>
50. J.J. Van Benschoten, J.Y. Lewis, W.R. Heineman, D.A. Roston, P.T. Kissinger, *J. Chem. Educ.* **60**, 772 (1983)
51. N.O. Laschuk, E.B. Easton, O.V. Zenkina, *RSC Adv.* **11**, 27925 (2021)
52. M. Balouiri, M. Sadiki, S.K. Ibsouda, *J. Pharm. Anal.* **6**, 71 (2016)
53. E. Urnuksaikhani, B.E. Bold, A. Gunbileg, N. Sukhbaatar, T. Mishig-Ochir, *Sci. Reports* **11**, 1 (2021)
54. T.C. Dakal, A. Kumar, R.S. Majumdar, V. Yadav, *Front. Microbiol.* **7**, 1831 (2016)
55. P. Kumar, P. Huo, R. Zhang, B. Liu, *Nanomaterials* **9**, 737 (2019)
56. D.-J. Scheffers, M.G. Pinho, *Microbiol. Mol. Biol. Rev.* **69**, 585 (2005)
57. C. Wu, G. Zhang, T. Xia, Z. Li, K. Zhao, Z. Deng, D. Guo, B. Peng, *Mater. Sci. Eng. C* **55**, 155 (2015)
58. A.K. Suresh, D.A. Pelletier, W. Wang, J.W. Moon, B. Gu, N.P. Mortensen, D.P. Allison, D.C. Joy, T.J. Phelps, M.J. Doktycz, *Environ. Sci. Technol.* **44**, 5210 (2010)
59. H. Barabadi, O. Hosseini, K. Jounaki, S. Sadeghian-Abadi, F. Ashouri, A. Mostafa AbdulabbasAlrikabi, H. Vahidi, S. Amidi, F. Mojab, N. Mohammadi, E. Mostafavi, *Mater. Adv.* **4**, 3037 (2023)

Springer Nature or its licensor (e.g. a society or other partner) holds exclusive rights to this article under a publishing agreement with the author(s) or other rightsholder(s); author self-archiving of the accepted manuscript version of this article is solely governed by the terms of such publishing agreement and applicable law.